

Enhanced Spin-Orbit Torques in Rare-Earth Pt/[Co/Ni]₂/Co/Tb Systems

Q.Y. Wong, C. Murapaka, W.C. Law, W.L. Gan, G.J. Lim, and W.S. Lew*

*School of Physical and Mathematical Sciences, Nanyang Technological University,
21 Nanyang Link, Singapore 637371*



(Received 21 August 2018; revised manuscript received 5 December 2018; published 22 February 2019)

We report the enhanced spin-orbit torque (SOT) effect due to the rare-earth metal Tb in a Pt/[Co/Ni]₂/Co/Tb multilayer with perpendicular magnetic anisotropy (PMA). Due to the large spin-orbit coupling in Tb, the effective dampinglike efficiency, ξ_{DL}^{eff} , is determined to be 0.55 for 9-nm Tb as compared to $\xi_{DL}^{eff} = 0.18$ for the reference Pt/[Co/Ni]₂/Co/Ta stack. A relatively large effective spin Hall efficiency of Tb, $\theta_{SH,Tb}^{eff}$, is determined to be -0.480 for Tb with a 9-nm thickness through a H_z -biased harmonic measurement. Enhanced magnetization switching efficiency is observed with increasing Tb thickness, affirming the sizable antidamping torque responsible for deterministic switching. Furthermore, due to a more substantial interfacial coupling in Co/Tb interface than in Co/Ta interface, strong angular dependence of the dampinglike and fieldlike terms is, but diminishes with increasing Tb thickness. These results affirm that Tb plays a significant role in tuning the SOT efficiency in these structures as the increased Tb concentration leads to an enhancement of the effective spin Hall angle and switching efficiency.

DOI: 10.1103/PhysRevApplied.11.024057

I. INTRODUCTION

Controlled manipulation of magnetization has brought about substantial advances in nonvolatile memory applications through current-induced magnetization reversal [1–6] and domain wall motion [7–12]. Current-induced spin-orbit torques (SOTs), which are attributed to the bulk spin Hall effect (SHE) [2,13–16] and the interfacial Rashba effect [1,17–19], open up alternatives for magnetization control [3,20]. SOT can be expressed as the dampinglike (DL) [21] and fieldlike (FL) [22] terms, where the DL torque originating from the SHE is responsible for reversal because of its antidamping form. The relative efficiency of the DL torque is a commonly used figure of merit for spin Hall material that relates proportionally to the effective spin Hall angle, $\xi_{DL}^{eff} \propto \theta_{SH}^{eff}$. The ongoing studies of 5d-transition heavy-metal (HM)–ferromagnetic (FM) interfaces has revealed strong intrinsic [23,24] spin Hall effects in Pt ($\theta_{SH,Pt}^{eff} = +0.09$) [2,25,26], β -Ta ($\theta_{SH,Ta}^{eff} = -0.12$) [2,27], and β -W ($\theta_{SH,W}^{eff} = -0.30$) [14]. We continue to pursue the search for alternate spin Hall materials from a class of elements that have been comparatively unexplored, the f -electron rare-earth (R) metals. The motivation for our work is based on the recent theoretical prediction that R metals have a substantial spin Hall effect contribution arising from large orbital angular momentum, l , and spin, s , due to their partially filled f orbitals [28,29]. More recently, several works have examined SOT

in R ferromagnets [30–41], which has gathered considerable attention in the field of spintronics. In Tb-based ferromagnets, Tb was used to provide antiferromagnetic coupling to compensate the magnetization in the Co-Tb alloys [32,39]. Ueda *et al.* [33] have reported large spin Hall efficiency in Pt/Co/Gd due to the presence of Gd, while Reynolds *et al.* [29] have characterized spin Hall efficiency of R metals such as Gd, Dy, Ho, Lu as the contributing interfacial layer on devices with in-plane magnetic anisotropy. Within the period of the Lanthanide series, Tb lies between Gd and Dy and has a $4f$ -level electronic configuration, which contributes to enhancing the spin Hall effect. Furthermore, Tb is considered chemically stable with partially filled f shells with spin Hall enhancing potential, but remains unexplored in terms of its spin Hall efficiency. Due to its similarity with other R metals explored earlier, it is intuitive that Tb is likely to enhance the SOTs. Bang *et al.* [31] have reported large interfacial SOT due to the Co/Tb interfaces in a Co/Tb multilayer structure from enhanced domain wall speed. In our study, the heterostructure of Pt/FM/Tb allows Tb to serve as a HM layer replacement for the enhancement of the SOT while enabling the quantification of the effective spin Hall efficiency in Tb. As such, Pt/FM/Tb structures should be explored further to determine their spin Hall efficiency.

We report the enhanced SOTs generated by the Co/Tb interface in a Pt/[Co/Ni]₂/Co/Tb system with perpendicular magnetic anisotropy (PMA) and strong azimuthal angle dependence via systematic variation of the Tb thickness from 5 to 9 nm. The results are compared with the control (reference) sample with a Ta cap layer. The

*wensiang@ntu.edu.sg

SOTs are characterized as a function of Tb thickness with a modified H_z -biased harmonic measurement setup. The magnitude of enhanced SOTs is contrasted by the magnitudes of their DL effective field, H_{DL} , FL effective field, H_{FL} , effective spin Hall angle, θ_{SH}^{eff} as well as the $J_{\text{threshold}}$ in the current-induced magnetization switching. Subsequently, the azimuthal angle dependence of the Pt/[Co/Ni]₂/Co/Tb (5–9 nm) stacks is also determined.

II. RESULTS AND DISCUSSIONS

The thin-film multilayers consisting of Ta(2 nm)/Pt(6 nm)/[Co(0.3 nm)/Ni(0.6 nm)]₂/Co(0.3 nm)/R(5–9 nm)/Ta(2 nm) and reference sample Ta(2 nm)/Pt(6 nm)/[Co(0.3 nm)/Ni(0.6 nm)]₂/Co(0.3 nm)/Ta(5 nm) are deposited onto thermally oxidized Si substrates using ultrahigh vacuum dc magnetron sputtering. Ta is used both as a bottom seed layer and capping layer to prevent oxidation of the Tb layer. Pt serves as an underlayer with (111) crystal orientation to promote PMA in the Co layer [6,42–44]. The deposition is carried out at room temperature under 3-mTorr Xe with a base pressure of 3×10^{-8} Torr. The Tb films capped with Ta exhibit electrical resistivity, $\rho_{\text{Tb}} = 108 \mu\Omega \text{ cm}$, indicating minimal oxidation of the Tb layer [45]. Figure 1(a) shows the schematic of the H_z -biased harmonic Hall measurement technique to estimate the effective fields. In this work, the Co/Tb interface is contrasted with the Co/Ta interface in terms of the SOT efficiency from the estimated effective fields and also from the current-induced magnetization switching.

The magnetic properties of the film structure, such as saturation magnetization, M_s , and the perpendicular anisotropic energy density, K_u , are determined from the vibrating sample magnetometer (VSM) measurements as shown in Fig. 1(b). K_u can be expressed as $K_u = H_k M_s / 2$ and $H_k = H_{\text{sat}} + 4\pi M_s$, where H_k is the anisotropy field and H_{sat} is the hard axis saturation field. All the films exhibit PMA induced by the bottom Pt/Co interface. As summarized in Fig. 1(b), M_s and K_u are both reduced with increasing Tb thickness suggesting that Tb is a critical factor in achieving strong PMA. When the thickness of Tb, t_{Tb} , is varied from 5 to 9 nm, it leads to a 54% reduction in the magnitudes of K_u and M_s . This suggests that the drop in the calculated K_u is significantly due to the reduction in the M_s value. The reduction in M_s value can potentially be due to compensation from the FM properties of Tb. From the experimental data, M_s for the Co/Ni multilayer stack decreases with increasing Tb thickness from 5 to 9 nm. The saturation magnetization decreases from 408 to 157 emu/cm³ for the film stacks with 5- and 9-nm Tb, respectively. The reference stack (Co/Ta) has a saturation magnetization of 596 emu/cm³. The decreases in M_s and H_k can be accounted for by the intermixing at the Co/Tb interface. Tb atomic layers adjacent to the Co have nonzero magnetic moments. These nonzero magnetic moments are

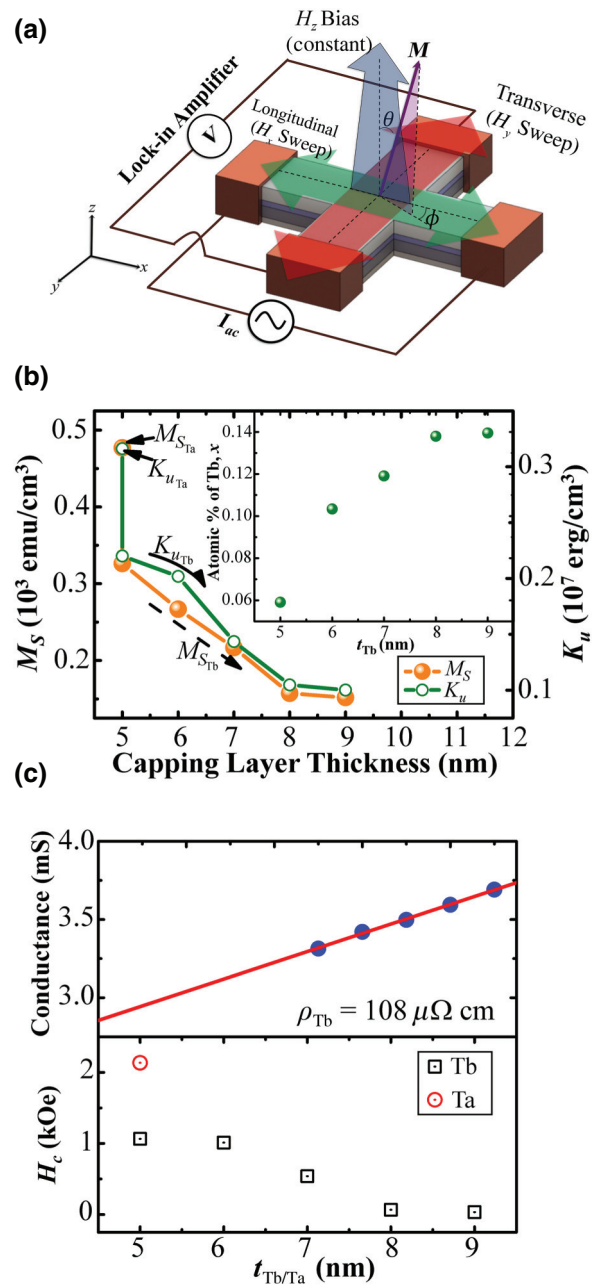


FIG. 1. (a) Schematic illustration of the H_z -biased measurement configuration for evaluation of the SOT in Cartesian coordinates. (b) Saturation magnetization (M_s) and perpendicular magnetic anisotropic energy density (K_u) vs capping layer thickness with percentage concentration of Tb in film stack inset. (c) Relation of channel Hall bar conductance and coercivity, H_c , with metallic-capping-layer thickness, $t_{\text{Tb/Ta}}$. The red line denotes a fit of linearity.

antiparallel to the Co/Ni layers, resulting in an antiferromagnetic coupling between Co and Tb. At the interface, the atomic moments of Co and Tb couple in an antiparallel arrangement such that the total net magnetization, M_s , of

$\text{Co}/\text{Ni}/\text{Co}_{1-x}\text{Tb}_x$ can be expressed as

$$M_s = (1 - x)M_{\text{Co}/\text{Ni}/\text{Co}} - xM_{\text{Tb}}, \quad (1)$$

where $M_{\text{Co}/\text{Ni}/\text{Co}}$ and M_{Tb} are the magnetizations of the ferromagnetically coupled Co/Ni multilayer adjacent to the closest neighboring Co and Tb, respectively, and x stands for the average atomic percentage of Tb in the entire film stack. Taking the M_s value from the reference film stack of 596 emu/cm³, without the influence of Tb and M_{Tb} as $8.9\mu_B$ [46], M_{Tb} can be determined from the atomic moment of Tb as follows, $M_{\text{Tb}} = N_A(\rho_{\text{Tb}}/A_{R,\text{Tb}})8.9\mu_B = 2587 \text{ emu/cm}^3$, where N_A is the Avogadro constant, ρ_{Tb} is the density of Tb, $A_{R,\text{Tb}}$ is the relative molecular mass of Tb, and μ_B is the Bohr magneton, respectively. The average ratio of Tb involved in the mixing increases with increasing thickness until it plateaus at 9-nm Tb. The most substantial proportion occurs at 14% when the thickness of Tb, t_{Tb} , is at 9 nm. With the trend of M_s and H_k observed, this methodology is adequate to account for the pattern of a compositional gradient at the Co/Tb interface. Similarly, due to the antiferromagnetic properties of Tb in the film stacks, the observed coercivity, H_c , decreases with increasing t_{Tb} .

A. Enhanced SOT fields in Rare-Earth Element Tb

Next, harmonic Hall voltage measurements are conducted by detecting Hall voltage variation as a function of the tilting of the magnetization under an in-plane field to quantify SOT effective fields. In these measurements, symmetrical Hall bars with dimensions of 5-μm width and 50-μm length are patterned using electron beam lithography and argon ion milling techniques. Electrical contact pads consisting of Ta (5 nm)/Cu (100 nm)/Ta(5 nm) are sputtered at the ends of the Hall bars to inject low-frequency ac current using a Keithley 6221 ac current source and using a 7265 Dual Phase DSP Lock-in Amplifier to detect the Hall voltage, V_H , while having a constant ±300 Oe H_z field as shown in the measurement geometry in Fig. 1(a). The presence of the H_z field enables the magnetization to remain at small polar angles for effective quantification of the SOT fields. The derivation of the modified harmonic measurements is found in the Supplemental Material [47]. Figure 1(c) indicates the relation between the coercitivity, H_c , and the capping layer thickness of Tb and Ta. Figures S2 and S3 of the Supplemental Material [47] show the VSM and the anomalous Hall resistance measurement for various t_{Tb} and their corresponding H_c , respectively. The quantification of Tb resistivity, ρ_{Tb} , is done by measuring the resistance of the Hall bar devices with various t_{Tb} and their conductances are plotted as a function of t_{Tb} as shown in the top graph of Fig. 1(c). The inverse of the gradient corresponds to $\rho_{\text{Tb}} = 108 \pm 2 \mu\Omega \text{ cm}$, while the vertical intersect corresponds to the conductance of the remaining part of the film stack. The current densities that

flow through the HM and R metal are accounted for by assuming the parallel resistance model of current distribution within the Hall cross device through the ratio of resistivities.

SOT harmonic measurements are carried out by passing ac current, I_{ac} , along the x direction with frequency, $\omega = 333$ Hz, in the presence of an additional H_z -biased field. The voltage measurement is recorded in two measurement schemes; the longitudinal and transverse schemes. The first and second harmonics, V_ω and $V_{2\omega}$, respectively, are concurrently measured from the Hall voltage using a lock-in amplifier and recorded as a function of the applied field H_x (H_y) as shown in Fig. 2. The modulation amplitudes of the polar, $\Delta\theta$, and azimuthal axes, $\Delta\phi$, for a H_z -biased measurement are determined to be (See derivation in Supplemental Material [47]):

$$\Delta\theta = \frac{(\Delta H_x \cos \phi + \Delta H_y \sin \phi)}{(H_{k,\text{eff}} + H_z)}, \quad (2)$$

$$\Delta\phi = \frac{\Delta H_y H_x - \Delta H_x H_y}{H_x^2 + H_y^2}, \quad (3)$$

where $H_{k,\text{eff}}$ is the effective anisotropic field of the material stack, H_z is the magnitude of the biased field, $\Delta H_x = H_{\text{DL}}$ and $\Delta H_y = H_{\text{FL}}$, and the H_x and H_y correspond to the in-plane field sweep in the harmonic measurement.

The coefficients of the first and second harmonics are expressed as

$$V_\omega = \frac{1}{2}I_{\text{ac}}[R_{\text{AHE}} \cos \theta + R_{\text{PHE}} \sin^2 \theta \sin 2\phi], \quad (4)$$

$$V_{2\omega} = -\frac{1}{2}I_{\text{ac}} \left(\frac{1}{2}[-R_{\text{AHE}} \sin \theta + R_{\text{PHE}} \sin 2\theta \sin 2\phi] \Delta\theta + R_{\text{PHE}} \sin^2 \theta \cos 2\phi \Delta\phi \right), \quad (5)$$

where R_{AHE} is the anomalous Hall resistance, R_{PHE} is the planar Hall resistance, and I_{ac} represents the current in the wire. By substituting Eqs. (2) and (3) into Eq. (5), the H_{DL} and H_{FL} can be estimated by utilizing the following relation by eliminating the $(H_{k,\text{eff}} + H_z)$ and I_{ac} terms:

$$H_{\text{DL}(\text{FL})} = -2 \left(\frac{dV_{2\omega}}{dH_{x(y)}} \right) / \left(\frac{d^2V_\omega}{dH_{x(y)}^2} \right). \quad (6)$$

Figures 2(a) and 2(b) show V_ω and $V_{2\omega}$ as a function of H_x for $t_{\text{Tb}} = 5$ nm with the initial magnetization state set to be $+M_z$ and $-M_z$, while Figs. 2(c) and 2(d) show V_ω and $V_{2\omega}$ as a function of H_y . $V_{2\omega}$ varies linearly for both H_x and H_y with similar slopes for H_x and is reversed for H_y when the initial magnetization state is reversed, which

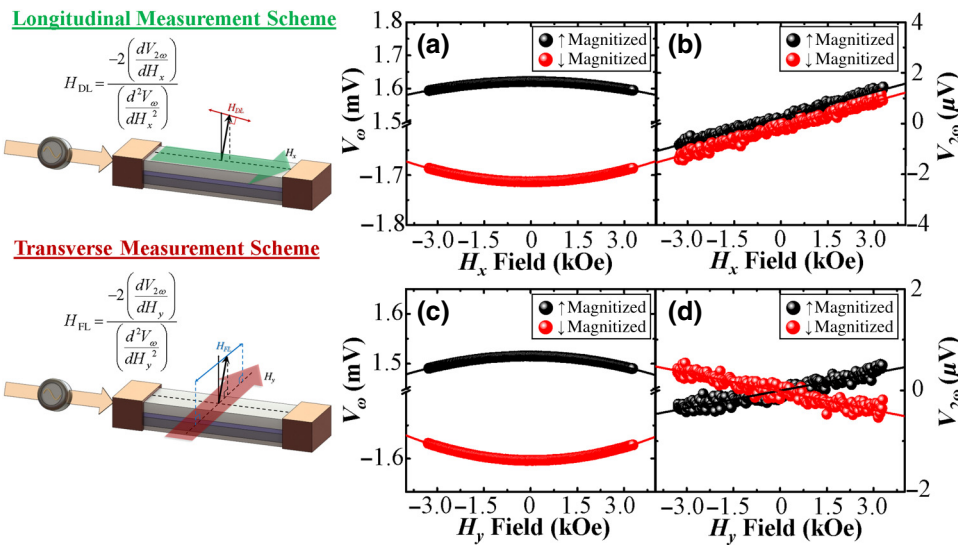


FIG. 2. (a) First harmonic voltage, V_ω , and (b) second harmonic voltage, $V_{2\omega}$, as a function of H_x in the longitudinal measurement scheme. (c) V_ω and (d) $V_{2\omega}$ as a function of H_y in the transverse measurement scheme. The measurement geometry of both measurement schemes is illustrated on the left of each corresponding plot.

is expected behavior from the H_{DL} and H_{FL} contributions [15,25,33,48,49].

The effects of Joule heating are negligible since the effective fields determined vary linearly with the input current density. The sign of H_{DL} is M_z dependent while the H_{FL} is independent of M_z , as previously reported [15,49]. To take into account the planar Hall effect component, the PHE correction factor, $\zeta = R_{PHE}/R_{AHE}$, can be used to correct the H_{DL} and H_{FL} given by the following relations [50]:

$$H_{DL, \text{corrected}} = \frac{H_{DL} + 2\zeta H_{FL}}{1 - 4\zeta^2}, \quad (7)$$

$$H_{FL, \text{corrected}} = \frac{H_{FL} + 2\zeta H_{DL}}{1 - 4\zeta^2}. \quad (8)$$

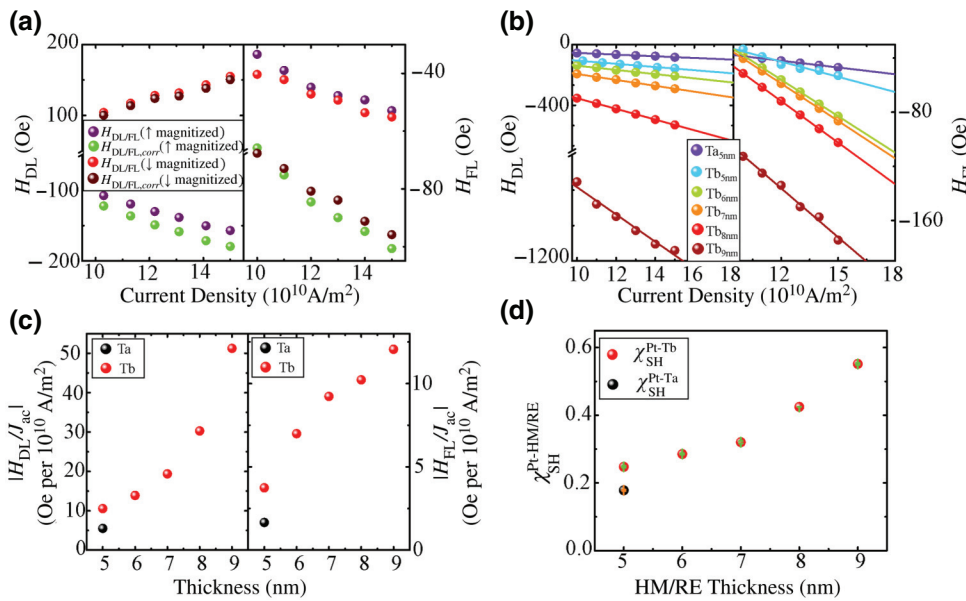
The PHE-corrected longitudinal $H_{DL, \text{corrected}}$ and transverse $H_{FL, \text{corrected}}$ fields, together with the H_{DL} and H_{FL} , are plotted as a function of current density in Fig. 3(a). The PHE correction factor, ζ , is determined via the relation related to the R_{AHE} :

$$\zeta = \frac{1}{2} \frac{(\partial^2 V_\omega / \partial H)_{\phi=-45^\circ} - (\partial^2 V_\omega / \partial H)_{\phi=45^\circ}}{(\partial^2 V_\omega / \partial H)_{\phi=-45^\circ} + (\partial^2 V_\omega / \partial H)_{\phi=45^\circ}}. \quad (9)$$

The values of the PHE correction for the HM or R metal thicknesses, $5 \text{ nm} \leq t_{Tb} \leq 9 \text{ nm}$, are calculated based on Eq. (9). The corrected values of the DL and FL fields are as shown in Fig. 3(a). $H_{DL, \text{corrected}}$ are contrasted with H_{DL} , and $H_{FL, \text{corrected}}$ are compared to the H_{FL} for $t_{Tb} = 5 \text{ nm}$. Hereafter, for simplicity, the corrected fields are called H_{DL} and H_{FL} . The corresponding PHE-correction values are shown in Table I.

The current-induced effective fields, H_{DL} and H_{FL} , increase linearly with the input, J_{ac} , as shown in Fig. 3(b).

and the effective fields per unit current density relation with capping layer thickness are shown in Fig. 3(c). $|H_{DL}/J_{ac}|$ and $|H_{FL}/J_{ac}|$ for the Tb series of films have significantly larger induced effective fields as compared to the Ta capping. $|H_{DL}/J_{ac}|$ increases considerably with increasing the Tb thickness from approximately 10 Oe per 10^{10} A/m^2 for $t_{Tb} = 5 \text{ nm}$ to approximately 51 Oe per 10^{10} A/m^2 for $t_{Tb} = 9 \text{ nm}$. The calculations are corrected based on the current distributions in the film stack, assuming that the Pt, Co, Ni, and Tb (Ta) layers act as resistances in parallel, such that the current flowing in each layer is distributed according to the resistivities. As the rest of the structure remains congruent throughout, the increase in current in Tb is the sole cause of the rise and is invariant with Pt thickness. Therefore, since $|H_{DL}/J_{ac}|$ increases with t_{Tb} as shown in Fig. 3(c), it is inferable that the Tb metal at the top interface produces a DL SOT that acts on the ferromagnetically coupled Co/Ni multilayer since the t_{Pt} remains the same for all film stacks. The SOT efficiency can be expressed as $\xi_{DL(FL)}^{\text{eff}} = 2eH_{DL(FL)}M_s/\hbar J_{ac}$, where $\xi_{DL(FL)}^{\text{eff}}$ is the SOT efficiency, $H_{DL(FL)}$ is the effective field, J_{ac} is the input ac current density, and M_s is the saturation magnetization. The enhancement of the $|H_{DL}/J_{ac}|$ is likely due to Tb having $\xi_{SH,Tb}^{\text{eff}}$ that is opposite in sign to Pt, such that the top and bottom interfaces have an additive effect, which gives rise to an effective DL efficiency, ξ_{DL}^{eff} . In Fig. 3(d), $|H_{FL}/J_{ac}|$ as a function of t_{Tb} shows that with increasing t_{Tb} , the FL term increases systematically by a factor of 2.3, indicating the enhancement of FL SOT caused by the presence of Tb. $|H_{FL}/J_{ac}|$ increases from approximately 2 Oe per 10^{10} A/m^2 for $t_{Tb} = 5 \text{ nm}$ to approximately 13 Oe per 10^{10} A/m^2 for $t_{Tb} = 9 \text{ nm}$. The FL efficiency calculated for $t_{Tb} = 5 \text{ nm}$ is $|\xi_{FL}^{\text{eff}}| = 0.12$ and for $t_{Tb} = 9 \text{ nm}$ it is $|\xi_{FL}^{\text{eff}}| = 0.05$. This shows that even though the magnitude of the FL term increases with Tb thickness, the overall efficiency of the FL term on the FM layer diminishes due to



the M_s . The DL efficiency, $|\xi_{DL}^{\text{eff}}|$, is approximately twice the FL efficiency, $|\xi_{FL}^{\text{eff}}|$, for $t_{\text{Tb}} = 5 \text{ nm}$ and this ratio of $|\xi_{DL}^{\text{eff}}|/|\xi_{FL}^{\text{eff}}|$ increases approximately one order of magnitude, that is, ten times. Therefore, these results indicate that SHE is likely the more dominant mechanism in the studied stack variation [51,52].

In this SHE-dominant system, we assume this mechanism is responsible for the DL term such that the ξ_{DL}^{eff} relates directly to the effective spin Hall angle of the Pt-Tb system, $\theta_{\text{SH}}^{\text{eff}}$, that is, $\xi_{DL}^{\text{eff}} \approx \theta_{\text{SH}}^{\text{eff}}$. As such, the magnitude of the effective spin Hall angle, $\theta_{\text{SH}}^{\text{eff}}$, is determined to range from $|\theta_{\text{SH,Ta}}^{\text{eff}}| \sim 0.18 \pm 0.01$ for the $t_{\text{Ta}} = 5 \text{ nm}$ capping layer and $|\theta_{\text{SH,Tb}}^{\text{eff}}| \sim 0.25 \pm 0.01$ for $t_{\text{Tb}} = 5 \text{ nm}$ to $|\theta_{\text{SH,Tb}}^{\text{eff}}| \sim 0.55 \pm 0.01$ for $t_{\text{Tb}} = 9 \text{ nm}$ as shown in Fig. 3(d). In this film stack, the growth of the Pt/Co interface not only serves as an underlying surface that promotes PMA, but it also affects the spin-mixing conductance as there may be intermixing and disorder at the Pt/Co interface [53]. The $\theta_{\text{SH,Tb}}^{\text{eff}}$ increases with the increasing influence of Tb. At larger t_{Tb} , the shunting of current in Pt greatly decreases; thus, this increases the contributing SHE from the Co/Tb interface. Therefore,

FIG. 3. (a) H_{DL} and $H_{DL,\text{corrected}}$, H_{FL} and $H_{FL,\text{corrected}}$ for a film stack with $t_{\text{Tb}} = 5 \text{ nm}$ as a function of the applied current density determined from the longitudinal and transverse harmonic measurement schemes, respectively. (b) H_{DL} and H_{FL} as a function of applied current density for various capping layer thicknesses for Tb (5–9 nm) and Ta (5 nm). (c) The absolute value of the effective fields per unit 10^{10} A/m^2 for $|H_{DL}/J_{ac}|$ and $|H_{FL}/J_{ac}|$. (d) Relation of SOT efficiency, $\xi_{SH}^{Pt-\text{HM}(R)}$, with a thickness of Ta and Tb.

taking the spin Hall angle of Pt, $\theta_{\text{SH,Pt}}^{\text{eff}} \approx +0.07$, from known literature [2,25,26], the reference sample gives rise to $\theta_{\text{SH,Ta}}^{\text{eff}} \approx -0.11$, which is within a reasonable range of the spin Hall angle reported for Ta [2,27]. Similarly, the spin Hall angle of Tb, $\theta_{\text{SH,Tb}}^{\text{eff}}$ can subsequently be derived from the ξ_{DL}^{eff} such that its value ranges from $-0.18 \leq \theta_{\text{SH,Tb}}^{\text{eff}} \leq -0.48$ for $5 \leq t_{\text{Tb}} \leq 9 \text{ nm}$.

B. Current-induced magnetization switching in Pt/[Co/Ni]₂/Co/Tb (5–9 nm) and reference sample Pt/[Co/Ni]₂/Co/Ta (5 nm)

Current-induced magnetization switching measurements are performed on the Hall cross structure. As expected, when a charge current passes through, a nonzero SOT is present due to the lack of inversion symmetry in Pt/[Co/Ni]₂/Co/Tb systems. The function of Hall resistance, R_H , against an in-plane dc current, I_{DC} , is determined through a constant in-plane magnetic field, H_x , applied along the x axis to overcome the rotational symmetry and assist in the magnetization reversal. Ten-ms current pulses are swept with varying magnitudes from -25 mA to $+25 \text{ mA}$, and the R - I loops observed reveal the change between two resistance states. The magnitude of change in resistance agrees with the observation in the R - H_z loops, indicating deterministic magnetization reversal between the $\pm z$ directions due to the current pulse. As shown in Fig. 4(a), the switching direction changes with the direction of the in-plane magnetic field; a clockwise loop is obtained for $-H_x$ and an anticlockwise loop is acquired for $+H_x$. This indicates the Slonczewski-like symmetry induces switching that is determined by the direction of H_x . Due to the sizable H_{DL} , SOT mainly originates from the SHE in both the Pt and Ta or Tb channels. When $H_x = 0$, magnetization switching diminishes as there is

TABLE I. Thicknesses of Tb and Ta and their corresponding PHE correction factors.

Thicknesses (nm)	R_{AHE}/Ω	$\zeta = R_{\text{PHE}}/R_{\text{AHE}}$
Tb 5	0.113	0.220
6	0.136	0.324
7	0.120	0.243
8	0.112	0.327
9	0.080	0.053
Ta 5	0.148	0.318

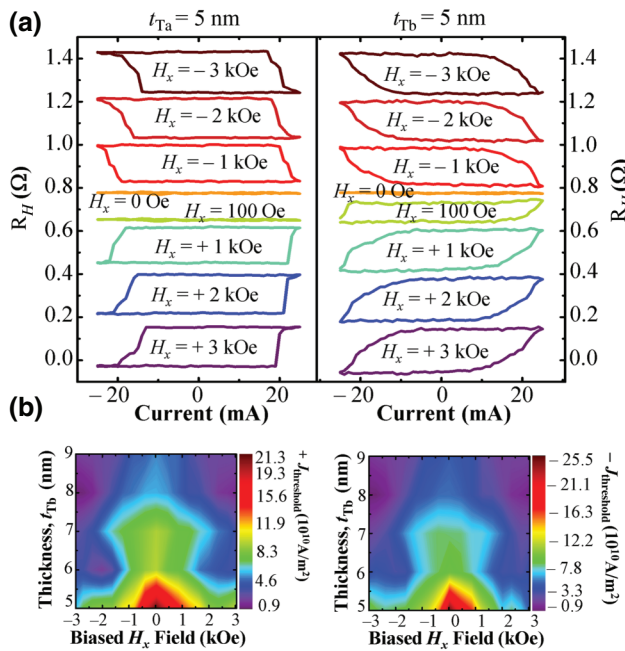


FIG. 4. (a) Current-induced magnetization switching curves for the reference sample, \$t_{\text{Ta}} = 5 \text{ nm}\$ and Tb-based sample, \$t_{\text{Tb}} = 5 \text{ nm}\$ structures measured with different in-plane external magnetic fields \$H_x\$. (b) Switching phase diagram for the film stacks variations from \$5 \text{ nm} \leq t_{\text{Tb}} \leq 9 \text{ nm}\$, where \$J_{\text{threshold}}\$ is the minimum current density required for magnetization switching to occur.

insufficient tilt of the magnetization such that it cannot assist SOT switching for both \$t_{\text{Ta}} = 5 \text{ nm}\$ and \$t_{\text{Tb}} = 5 \text{ nm}\$. For the Tb sample, the polarity of the FM layer can be switched with low \$H_x\$ such that \$H_x < 100 \text{ Oe}\$. The results reveal that substantial antidamping torque enhanced by Tb causes a deterministic change of magnetization polarity in the device. The corresponding phase diagram of the various Tb thicknesses shown in Fig. 4(b) illustrate the behavior of threshold switching current density, \$J_{\text{threshold}}\$, in relation to the thickness of Tb and \$H_x\$. Here, \$J_{\text{threshold}}\$ is defined as the threshold current density at which magnetization switching originates and that corresponds to an initial abrupt jump in the resistance of the \$R\$-\$I\$ loop. In this SOT regime, the change of resistance in the \$R\$-\$I\$ loop is comparable to the AHE measurement, demonstrating that deterministic switching of Tb-based Co/Ni systems are possible and effective. At \$H_x = 100 \text{ Oe}\$, the reference sample is unable to switch the magnetization polarity, while the \$t_{\text{Tb}} = 5 \text{ nm}\$ sample is able to effectively switch at least 60% of the entire magnetization at the Hall cross. The results affirm that the Co/Tb interface is indeed responsible for the enhanced SOT generation due to the presence of a sizable antidamping torque. This is consistent with the earlier characterized \$H_{\text{DL}}\$ for the reference and the Tb samples, where the DL field for the \$t_{\text{Tb}} = 5 \text{ nm}\$ is twice that of that of the \$t_{\text{Ta}} = 5 \text{ nm}\$. For various Tb thicknesses,

the \$J_{\text{threshold}}\$ phase diagram shown in Fig. 4(b) has an optimum magnitude of \$J_{\text{threshold}}\$ in the blue and purple regions. These current densities in the area correspond to equal orders of magnitude for the spin-transfer torque (STT) switching mechanism [54]. For a low in-plane bias field, the optimum Tb thicknesses for effective switching varies between 7 to 9 nm, with applied in-plane biased fields \$H_x < 1000 \text{ Oe}\$. The Tb-based devices are capable of deterministic switching with a relatively small in-plane bias field along with low \$J_{\text{threshold}}\$ as compared to the reference sample.

C. Angular dependence of SOT fields in Pt/[Co/Ni]₂/Co/Tb (5–9 nm) and reference sample Pt/[Co/Ni]₂/Co/Ta (5 nm)

The angular dependence of the SOT fields is conducted to determine its relation with the azimuthal angle, \$\phi_H = \phi\$, between current direction and the magnetization in Tb-based PMA samples similar to the BaTiO₃ (BTO) samples [55]. The \$V_\omega\$ and \$V_{2\omega}\$ are measured at different azimuthal angle values with magnetization set to be in the \$-z\$ orientation for all measurements. The current density is set at \$1 \times 10^{11} \text{ A/m}^2\$ in the wire to have a better signal-to-noise ratio without compromising the Joule heating effects. At each azimuthal angle field sweep, the values \$A_\omega = \partial^2 V_\omega / \partial H^2\$ and \$B_{2\omega} = \partial V_{2\omega} / \partial H\$ are determined, and the function of \$A_\omega\$ against \$\phi_H\$ and \$B_{2\omega}\$ against \$\phi_H\$ are as shown in Figs. 5(a) and 5(b), respectively. As shown in Fig. 5(a), \$A_\omega\$ exhibits an evident \$-\sin 2\phi\$ behavior as predicted and \$B_{2\omega}\$ depicts a \$-\cos \phi\$ trend. This trend relates itself to the initial state of magnetization of the sample, such that the pattern will have a positive behavior of \$\sin 2\phi\$ and \$\cos \phi\$. By eliminating the dependence on \$I_{\text{ac}}\$, \$H_z\$, and \$H_{k,\text{eff}}\$, the ratio of \$\beta_\phi = B_{2\omega}/A_\omega\$ is computed and plotted in Fig. 5(c). A fitting function can be used to determine the mean SOT effective fields,

$$\begin{aligned} \beta_\phi = & \left(-\frac{1}{2} \sin \phi + \frac{\zeta \cos \phi \cos 2\phi}{1 - 2\zeta \sin 2\phi} \right) \Delta H_{\text{FL}} \\ & + \left(-\frac{1}{2} \cos \phi - \frac{\zeta \sin \phi \cos 2\phi}{1 - 2\zeta \sin 2\phi} \right) \Delta H_{\text{DL}}, \end{aligned} \quad (10)$$

$$\beta_\phi = a \Delta H_{\text{FL}} + b \Delta H_{\text{DL}}. \quad (11)$$

Using the fitting of Eq. (10) on the function of \$\beta_\phi\$ against \$\phi\$ on Fig. 5(c), the mean values of the DL term and FL term are determined to be \$35 \pm 2 \text{ Oe per } 10^{10} \text{ A/m}^2\$ and \$6 \pm 2 \text{ Oe per } 10^{10} \text{ A/m}^2\$, respectively, for \$t_{\text{Tb}} = 8 \text{ nm}\$ with \$\zeta = 0.327\$, which is consistent with the values determined through the harmonic measurements based on Eq. (9). To evaluate the SOT fields on an azimuthal angle for the variation of Tb thicknesses, the SOT fields are calculated based

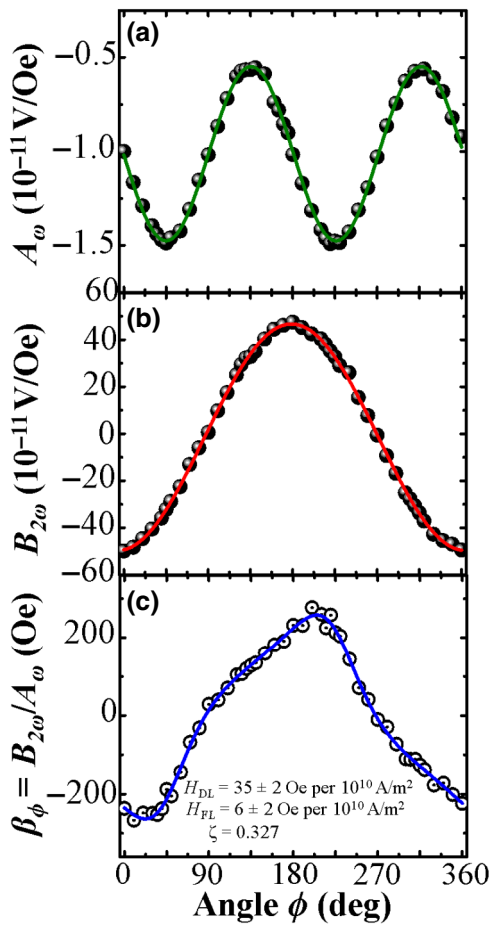


FIG. 5. A sample of $t_{Tb} = 8$ nm magnetized in the $-z$ orientation. (a) Second derivative of the parabolic first-harmonic Hall voltage as a function of azimuthal angle, ϕ , with $-\sin 2\phi$ fit. (b) The first derivative of the second-harmonic Hall voltage as a function of azimuthal angle, ϕ , with $-\cos \phi$. (c) β_ϕ as a function of the azimuthal angle, ϕ , and a fit from Eq. (10).

on the analytical expressions given by [56]

$$\Delta H_{DL} = \frac{b\beta_\phi - a\beta_{90-\phi}}{b^2 - a^2} \quad (12)$$

$$\Delta H_{FL} = \frac{a\beta_\phi - b\beta_{90-\phi}}{a^2 - b^2} \quad (13)$$

where a and b are coefficients related to Eq. (10) and are dependent on the orientation of the applied magnetic field, ϕ , and the PHE correction factor, ζ . It is noted that there exists a mirror symmetry at $\phi = 45^\circ$ such that $a(\zeta, \phi) = b'(\zeta, 90 - \phi)$ and $b(\zeta, \phi) = a'(\zeta, 90 - \phi)$ [55].

The symmetrical axes are indicated in red dashed lines as shown in Fig. 6. At these axes, there is no effective field computed as $a^2 = b^2$ cancels out the function at multiples of $\phi = 45^\circ$. As shown in Fig. 6, there are clear indications of the azimuthal angular dependence of both the DL

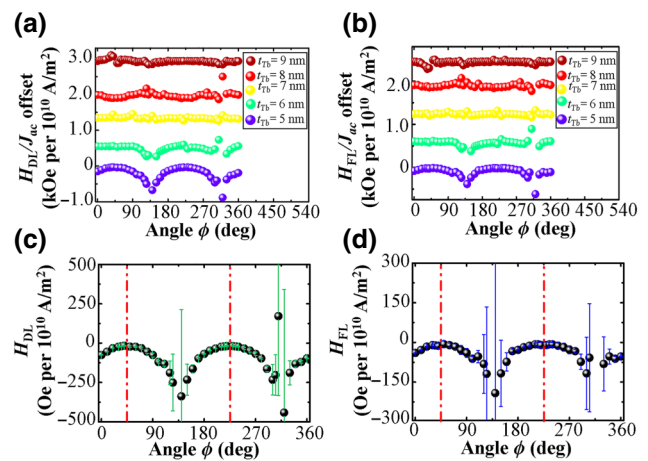


FIG. 6. Computed SOT-effective fields for the Tb samples ranging from $5 \text{ nm} \leq t_{Tb} \leq 9 \text{ nm}$ as a function of ϕ : (a) DL-effective field according to Eq. (12). (b) Consolidated FL-effective field according to Eq. (13). The dashed lines represent regions where no effective fields are computed at the symmetrical axes. (c) DL-effective field and (d) FL-effective field for $t_{Tb} = 5 \text{ nm}$.

term and the FL term, in which their mean values are determined to be 10 and 2 Oe/ 10^{10} A/m 2 , which is similar to the values obtained at 0° and 90° , respectively. Two minimums are observed at azimuthal angles of 45° and 225° , which indicates the angular dependence of the DL term in Pt/[Co/Ni] $_2$ /Co/Tb/Ta. Similarly, the FL term has minimums at the same angle, also indicating the angular dependence of the FL term. The angular dependence of the DL term is nontrivial and can be attributed to the combined effects of the Fermi surface distortion and Fermi sea contribution at the intermediate Rashba regime at the Co/Tb interface [56–58]. The angular dependence of the FL term is attributed to the Fermi surface distortion, which becomes significant when the Rashba spin-orbit coupling energy is comparable to the exchange energy [57]. In the Pt/[Co/Ni] $_2$ /Co/Ta reference sample, there is no indication of angular dependence as expected due to the weak Rashba spin-orbit coupling caused by oxidation of the top Ta layer [56,57]. Since angular dependence is absent in the reference sample and present in the samples with Co/Tb interfaces, it can be mentioned that the presence of strong Rashba spin coupling at the Co/Tb interface contributes to both DL and FL effective fields.

Comparing with the t_{Tb} , the angular dependences of both the DL term and FL term decrease with the increase in Tb thickness. At $t_{Tb} = 5$ nm, there is an indication of the angular dependence of both the DL and FL terms, but this dependence on magnetization direction diminishes with increasing thickness. This occurs due to the diminishing ratio of Rashba spin-orbit coupling to the exchange coupling of the magnetic material [56]. The diminishing

ratio of the Rashba spin-orbit coupling to exchange coupling could originate from one of these or a combination of these mechanisms, which disrupts the quality of the Co/Tb interface. First, the shift toward poor crystallinity [57] in thicker Tb samples, second, the increase in oxidation [56] of thicker Tb at the side walls of the Hall cross, and third, greater intermixing between Co and Tb at the Co/Tb interface can lead to the diminishing of the Rashba coupling. This dependence of the Rashba coupling on the Tb thickness was previously determined from the FL-efficiency in the H_z -biased harmonic measurement. Even as $\xi_{\text{FL}}^{\text{eff}}$ drops with increasing t_{Tb} , the $\xi_{\text{FL}}^{\text{eff}}$ for Co/Tb stacks are still more significant in magnitude than $\xi_{\text{FL}}^{\text{eff}}$ in the reference Co/Ta, which affirms that Tb is responsible for greater Rashba coupling leading to larger $\xi_{\text{FL}}^{\text{eff}}$.

III. CONCLUSION

We conclusively report the enhancement of the DL torque and FL torque on a perpendicularly magnetized Pt/[Co/Ni]₂/Co/Tb sample ($|\xi_{\text{DL}}^{\text{eff}}| \approx 0.25 \pm 0.01$ for $t_{\text{Tb}} = 5 \text{ nm}$) as compared to a reference Pt/[Co/Ni]₂/Co/Ta sample ($|\xi_{\text{DL}}^{\text{eff}}| \approx 0.18 \pm 0.01$ for $t_{\text{Tb}} = 5 \text{ nm}$), which is attributed to the sizeable spin-orbit coupling in *R* metal Tb. Due to a SHE-dominant mechanism, the $|\xi_{\text{DL}}^{\text{eff}}|$ increases to 0.55 ± 0.01 , but $|\xi_{\text{FL}}^{\text{eff}}|$ diminishes with increasing t_{Tb} , characterized using a H_z -bias harmonic Hall measurement. The current-induced magnetization switching shows that the enhanced DL term enables successful deterministic switching with the greatest efficiency when $t_{\text{Tb}} > 7 \text{ nm}$. Due to a stronger Rashba coupling in Co/Tb as compared to the reference Co/Ta, angular dependence of the DL and FL terms is observed for the Tb samples, while the reference stack has no angular dependence. In the Tb thickness variation, we report that the Rashba coupling diminishes with increasing thickness, which could be due to oxidation in the Tb sidewalls, poor crystallinity of Tb, and the increase in Co/Tb intermixing at the Co/Tb interface, which disrupts the Co/Tb interface. In summary, the enhancement of the DL and FL terms by *R* metal Tb opens up alternate potential avenues of research on *R* materials as spin Hall material alternatives for SOT-based devices.

ACKNOWLEDGMENTS

The work was supported by the Singapore National Research Foundation, Prime Minister's Office under a Competitive Research Programme (Non-volatile Magnetic Logic and Memory Integrated Circuit Devices, NRF-CRP9-2011-01), and an Industry-IHL Partnership Program (NRF2015-IIP001-001). The supports from an RIE2020 AME IAF-ICP Grant (I1801E0030) and a Programmatic Grant (No. A1687b0033) are also acknowledged. WSL is a member of the Singapore Spintronics Consortium (SG-SPIN).

- [1] I. M. Miron, G. Gaudin, S. Auffret, B. Rodmacq, A. Schuhl, S. Pizzini, J. Vogel, and P. Gambardella, Current-driven spin torque induced by the Rashba effect in a ferromagnetic metal layer, *Nat. Mater.* **9**, 230 (2010).
- [2] L. Liu, C. F. Pai, Y. Li, H. W. Tseng, D. C. Ralph, and R. A. Buhrman, Spin-torque switching with the giant spin Hall effect of tantalum, *Science* **336**, 555 (2012).
- [3] L. Liu, O. J. Lee, T. J. Gudmundsen, D. C. Ralph, and R. A. Buhrman, Current-Induced Switching of Perpendicularly Magnetized Magnetic Layers Using Spin Torque from the Spin Hall Effect, *Phys. Rev. Lett.* **109**, 096602 (2012).
- [4] L. Liu, C.-F. Pai, D. Ralph, and R. Buhrman, Magnetic Oscillations Driven by the Spin Hall Effect in 3-Terminal Magnetic Tunnel Junction Devices, *Phys. Rev. Lett.* **109**, 186602 (2012).
- [5] C. O. Avci, K. Garello, I. M. Miron, G. Gaudin, S. Auffret, O. Boulle, and P. Gambardella, Magnetization switching of an MgO/Co/Pt layer by in-plane current injection, *Appl. Phys. Lett.* **100**, 212404 (2012).
- [6] S. Li, S. Goolaup, J. Kwon, F. Luo, W. Gan, and W. S. Lew, Deterministic spin-orbit torque induced magnetization reversal in Pt/[Co/Ni] n/Co/Ta multilayer Hall bars, *Sci. Rep.* **7**, 972 (2017).
- [7] A. Yamaguchi, T. Ono, S. Nasu, K. Miyake, K. Mibu, and T. Shinjo, Real-Space Observation of Current-Driven Domain Wall Motion in Submicron Magnetic Wires, *Phys. Rev. Lett.* **92**, 077205 (2004).
- [8] M. Hayashi, L. Thomas, Y. B. Bazaliy, C. Rettner, R. Moriya, X. Jiang, and S. S. Parkin, Influence of Current on Field-Driven Domain Wall Motion in Permalloy Nanowires from Time Resolved Measurements of Anisotropic Magnetoresistance, *Phys. Rev. Lett.* **96**, 197207 (2006).
- [9] S. S. Parkin, M. Hayashi, and L. Thomas, Magnetic domain-wall racetrack memory, *Science* **320**, 190 (2008).
- [10] I. M. Miron, T. Moore, H. Szambolics, L. D. Budapesteanu, S. Auffret, B. Rodmacq, S. Pizzini, J. Vogel, M. Bonfim and, and A. Schuhl, Fast current-induced domain-wall motion controlled by the Rashba effect, *Nat. Mater.* **10**, 419 (2011).
- [11] V. E. Demidov, S. Urazhdin, H. Ulrichs, V. Tiberkevich, A. Slavin, D. Baither, G. Schmitz, and S. O. Demokritov, Magnetic nano-oscillator driven by pure spin current, *Nat. Mater.* **11**, 1028 (2012).
- [12] S. Emori, E. Martinez, K.-J. Lee, H.-W. Lee, U. Bauer, S.-M. Ahn, P. Agrawal, D. C. Bono, and G. S. D. Beach, Spin Hall torque magnetometry of Dzyaloshinskii domain walls, *Phys. Rev. B* **90**, 184427 (2014).
- [13] Y. Tserkovnyak, A. Brataas, and G. E. Bauer, Theory of current-driven magnetization dynamics in inhomogeneous ferromagnets, *J. Magn. Magn. Mater.* **320**, 1282 (2008).
- [14] C.-F. Pai, L. Liu, Y. Li, H. W. Tseng, D. C. Ralph, and R. A. Buhrman, Spin transfer torque devices utilizing the giant spin Hall effect of tungsten, *Appl. Phys. Lett.* **101**, 122404 (2012).
- [15] S. Emori, U. Bauer, S.-M. Ahn, E. Martinez, and G. S. Beach, Current-driven dynamics of chiral ferromagnetic domain walls, *Nat. Mater.* **12**, 611 (2013).

- [16] P. Haazen, E. Murè, J. Franken, R. Lavrijsen, H. Swagten, and B. Koopmans, Domain wall depinning governed by the spin Hall effect, *Nat. Mater.* **12**, 299 (2013).
- [17] D. Pesin and A. MacDonald, Quantum kinetic theory of current-induced torques in Rashba ferromagnets, *Phys. Rev. B* **86**, 014416 (2012).
- [18] K.-W. Kim, S.-M. Seo, J. Ryu, K.-J. Lee, and H.-W. Lee, Magnetization dynamics induced by in-plane currents in ultrathin magnetic nanostructures with Rashba spin-orbit coupling, *Phys. Rev. B* **85**, 180404 (2012).
- [19] X. Wang and A. Manchon, Diffusive Spin Dynamics in Ferromagnetic Thin Films with a Rashba Interaction, *Phys. Rev. Lett.* **108**, 117201 (2012).
- [20] I. M. Miron, G. Gaudin, P. J. Zermatten, M. V. Costache, S. Auffret, S. Bandiera, B. Rodmacq, A. Schuhl, and P. Gambardella, Perpendicular switching of a single ferromagnetic layer induced by in-plane current injection, *Nature* **476**, 189 (2011).
- [21] J. C. Slonczewski, Current-driven excitation of magnetic multilayers, *J. Magn. Magn. Mater.* **159**, L1 (1996).
- [22] S. Zhang, P. Levy, and A. Fert, Mechanisms of Spin-Polarized Current-Driven Magnetization Switching, *Phys. Rev. Lett.* **88**, 236601 (2002).
- [23] T. Tanaka, H. Kontani, M. Naito, T. Naito, D. S. Hirashima, K. Yamada, and J. Inoue, Intrinsic spin Hall effect and orbital Hall effect in 4d and 5d transition metals, *Phys. Rev. B* **77**, 165117 (2008).
- [24] E. M. Chudnovsky, Intrinsic spin Hall effect in noncubic crystals, *Phys. Rev. B* **80**, 153105 (2009).
- [25] S. Woo, M. Mann, A. J. Tan, L. Caretta, and G. S. Beach, Enhanced spin-orbit torques in Pt/Co/Ta heterostructures, *Appl. Phys. Lett.* **105**, 212404 (2014).
- [26] P. Sethi, S. Krishnia, S. H. Li, and W. S. Lew, Modulation of spin-orbit torque efficiency by thickness control of heavy metal layers in Co/Pt multilayers, *J. Magn. Magn. Mater.* **426**, 497 (2017).
- [27] Q. Y. Wong, W. L. Gan, F. L. Luo, G. J. Lim, C. C. I. Ang, F. N. Tan, W. C. Law, and W. S. Lew, In-situ Kerr and harmonic measurement in determining current-induced effective fields in MgO/CoFeB/Ta, *J. Phys. D: Appl. Phys.* **51**, 115004 (2018).
- [28] T. Tanaka and H. Kontani, Intrinsic spin and orbital Hall effects in heavy-fermion systems, *Phys. Rev. B* **81**, 224401 (2010).
- [29] N. Reynolds, P. Jadaun, J. T. Heron, C. L. Jermain, J. Gibbons, R. Collette, R. A. Buhrman, D. G. Schlom, and D. C. Ralph, Spin Hall torques generated by rare-earth thin films, *Phys. Rev. B* **95**, 064412 (2017).
- [30] Z. Zhao, M. Jamali, A. K. Smith, and J.-P. Wang, Spin Hall switching of the magnetization in Ta/TbFeCo structures with bulk perpendicular anisotropy, *Appl. Phys. Lett.* **106**, 132404 (2015).
- [31] D. Bang, J. Yu, X. Qiu, Y. Wang, H. Awano, A. Manchon, and H. Yang, Enhancement of spin Hall effect induced torques for current-driven magnetic domain wall motion: Inner interface effect, *Phys. Rev. B* **93**, 174424 (2016).
- [32] J. Finley and L. Liu, Spin-Orbit-Torque Efficiency in Compensated Ferrimagnetic Cobalt-Terbium Alloys, *Phys. Rev. Appl.* **6**, 054001 (2016).
- [33] K. Ueda, C.-F. Pai, A. J. Tan, M. Mann, and G. S. Beach, Effect of rare earth metal on the spin-orbit torque in magnetic heterostructures, *Appl. Phys. Lett.* **108**, 232405 (2016).
- [34] K. Ueda, M. Mann, C.-F. Pai, A.-J. Tan, and G. S. D. Beach, Spin-orbit torques in Ta/Tb_xCo_{100-x} ferrimagnetic alloy films with bulk perpendicular magnetic anisotropy, *Appl. Phys. Lett.* **109**, 232403 (2016).
- [35] N. Roschewsky, T. Matsumura, S. Cheema, F. Hellman, T. Kato, S. Iwata, and S. Salahuddin, Spin-orbit torque switching of ultralarge-thickness ferrimagnetic GdFeCo, *Appl. Phys. Lett.* **109**, 112403 (2016).
- [36] K. Ueda, M. Mann, P. W. P. de Brouwer, D. Bono, and G. S. D. Beach, Temperature dependence of spin-orbit torques across the magnetic compensation point in a ferrimagnetic TbCo alloy film, *Phys. Rev. B* **96**, 064410 (2017).
- [37] N. Roschewsky, C.-H. Lambert, and S. Salahuddin, Spin-orbit torque switching of ultralarge-thickness ferrimagnetic GdFeCo, *Phys. Rev. B* **96**, 064406 (2017).
- [38] R. Mishra, J. Yu, X. Qiu, M. Motapothula, T. Venkatesan, and H. Yang, Anomalous Current-Induced Spin Torques in Ferrimagnets near Compensation, *Phys. Rev. Lett.* **118**, 167201 (2017).
- [39] S.-G. Je, J.-C. Rojas-Sánchez, T. H. Pham, P. Vallobra, G. Malinowski, D. Lacour, T. Fache, M. C. Cyrille, D.-Y. Kim, S.-B. Choe, M. Belmeguenai, M. Hehn, S. Mangin, G. Gaudin, and O. Boulle, Spin-orbit torque-induced switching in ferrimagnetic alloys: Experiments and modeling, *Appl. Phys. Lett.* **112**, 062401 (2018).
- [40] T. H. Pham, S.-G. Je, P. Vallobra, T. Fache, D. Lacour, G. Malinowski, M. C. Cyrille, G. Gaudin, O. Boulle, M. Hehn, J.-C. Rojas-Sánchez, and S. Mangin, Thermal Contribution to the Spin-Orbit Torque in Metallic-Ferrimagnetic Systems, *Phys. Rev. Appl.* **9**, 064032 (2018).
- [41] T.-C. Wang, T.-Y. Chen, C.-T. Wu, H.-W. Yen, and C.-F. Pai, Comparative study on spin-orbit torque efficiencies from W/ferromagnetic and W/ferrimagnetic heterostructures, *Phys. Rev. Mater.* **2**, 014403 (2018).
- [42] M. Johnson, P. Bloemen, F. Den Broeder, and J. De Vries, Magnetic anisotropy in metallic multilayers, *Rep. Prog. Phys.* **59**, 1409 (1996).
- [43] H. Kurt, M. Venkatesan, and J. Coey, Enhanced perpendicular magnetic anisotropy in Co/Ni multilayers with a thin seed layer, *J. Appl. Phys.* **108**, 073916 (2010).
- [44] C. Engel, S. Goolaup, F. Luo, W. Gan, and W. S. Lew, Spin-orbit torque induced magnetization anisotropy modulation in Pt/(Co/Ni)₄/Co/IrMn heterostructure, *J. Appl. Phys.* **121**, 143902 (2017).
- [45] S. Arajs and R. V. Colvin, Thermal conductivity and electrical resistivity of terbium between 5 and 300 K, *Phys. Rev.* **136**, A439 (1964).
- [46] T. O. Brun and G. H. Lander, Magnetic form factor of terbium in Tb(OH)₃, *Phys. Rev. B* **9**, 3003 (1974).
- [47] See Supplemental Material at <http://link.aps.org/supplemental/10.1103/PhysRevApplied.11.024057> for the detailed analytical derivation of the current induced fields, angular dependence in the H_z -biased harmonic Hall measurements and the detailed VSM and AHE loops for various thickness of Tb.
- [48] J. Kim, J. Sinha, M. Hayashi, M. Yamanouchi, S. Fukami, T. Suzuki, S. Mitani, and H. Ohno, Layer thickness dependence of the current-induced effective field vector in Ta/CoFeB|MgO, *Nat. Mater.* **12**, 240 (2013).

- [49] J. Torrejon, J. Kim, J. Sinha, S. Mitani, M. Hayashi, M. Yamanouchi, and H. Ohno, Interface control of the magnetic chirality in CoFeB/MgO heterostructures with heavy-metal underlayers, *Nat. Commun.* **5**, 4655 (2014).
- [50] M. Hayashi, J. Kim, M. Yamanouchi, and H. Ohno, Quantitative characterization of the spin-orbit torque using harmonic Hall voltage measurements, *Phys. Rev. B* **89**, 144425 (2014).
- [51] P. M. Haney, H.-W. Lee, K.-J. Lee, A. Manchon, and M. D. Stiles, Current-induced torques and interfacial spin-orbit coupling, *Phys. Rev. B* **88**, 214417 (2013).
- [52] K. W. Kim, H. W. Lee, K. J. Lee, and M. D. Stiles, Chirality from Interfacial Spin-Orbit Coupling Effects in Magnetic Bilayers, *Phys. Rev. Lett.* **111**, 216601 (2013).
- [53] C.-F. Pai, Y. Ou, L. H. Vilela-Leão, D. C. Ralph, and R. A. Buhrman, Dependence of the efficiency of spin Hall torque on the transparency of Pt/ferromagnetic layer interfaces, *Phys. Rev. B* **92**, 064426 (2015).
- [54] S. Ikeda, K. Miura, H. Yamamoto, K. Mizunuma, H. D. Gan, M. Endo, S. Kanai, J. Hayakawa, F. Matsukura and, and H. Ohno, A perpendicular-anisotropy CoFeB–MgO magnetic tunnel junction, *Nat. Mater.* **9**, 721 (2010).
- [55] C. Engel, S. Goolaup, F. Luo, and W. S. Lew, Quantitative characterization of spin-orbit torques in Pt/Co/Pt/Co/Ta/BTO heterostructures due to the magnetization azimuthal angle dependence, *Phys. Rev. B* **96**, 054407 (2017).
- [56] C. Ortiz Pauyac, X. Wang, M. Chshiev, and A. Manchon, Angular dependence and symmetry of Rashba spin torque in ferromagnetic heterostructures, *Appl. Phys. Lett.* **102**, 252403 (2013).
- [57] K.-S. Lee, D. Go, A. Manchon, P. M. Haney, M. D. Stiles, H.-W. Lee, and K.-J. Lee, Angular dependence of spin-orbit spin-transfer torques, *Phys. Rev. B* **91**, 144401 (2015).
- [58] F. Mahfouzi and N. Kioussis, First-principles study of the angular dependence of the spin-orbit torque in Pt/Co and Pd/Co bilayers, *Phys. Rev. B* **97**, 224426 (2018).